Applied Clay Science 150 (2017) 115–124

Contents lists available at ScienceDirect

Applied Clay Science

journal homepage: www.elsevier.com/locate/clay

Research paper

Insights into the formation mechanism of imogolite from a full-range observation of its sol-gel growth

Peixin Du[a,b], Peng Yuan[a,b,*], Antoine Thill[c], Faïza Annabi-Bergaya[d], Dong Liu[a,b], Shun Wang[a,b]

[a] CAS Key Laboratory of Mineralogy and Metallogeny/Guangdong Provincial Key Laboratory of Mineral Physics and Materials, Guangzhou Institute of Geochemistry, Chinese Academy of Sciences, 511 Kehua Street, Guangzhou 510640, China
[b] University of Chinese Academy of Sciences, 19 Yuquan Road, Beijing 100049, China
[c] LIONS, NIMBE, CEA, CNRS, Université Paris-Saclay, Gif sur Yvette 91191, France
[d] Interfaces, Confinement, Matériaux et Nanostructures (ICMN, UMR CNRS 7374), 1b Rue de la Férollerie, Orléans Cedex 2 45071, France

ARTICLE INFO

Keywords:
Imogolite
Allophane
Growth
Hydroxyaluminosilicate
Soil

ABSTRACT

Imogolite (Imo) was prepared via a sol-gel method. The time-dependent changes in its morphology, structure and texture during the whole synthesis process (from amorphous precursors to the final products through nanoscale intermediates) were monitored by atomic force microscopy (AFM), X-ray diffraction (XRD), Fourier transform infrared (FTIR) spectroscopy, nuclear magnetic resonance (NMR) and N_2 physisorption. The results showed that a shape transition from a spherical open imogolite local structure (ImoLS) to a tubular open ImoLS occurred in the process of proto-imogolite (proto-Imo) formation. Based on the overall structure of the obtained solid products and the occurring main reactions, Imo synthesis process was described in five steps: i) formation of amorphous precursors by hydrolysis and condensation of Al and Si; ii) formation of proto-Imo with an open ImoLS at the expense of the amorphous precursors; iii) open ImoLS dominates; it grows and assembles into the first closed ImoLS (tubes and spheres); iv) closed ImoLS dominates and continues to form (mainly tubes) at the expense of open ImoLS; and v) no more open ImoLS; further growth of already-formed Imo via oriented aggregation. These findings provide new insights into the formation mechanism and structure of proto-Imo and Imo, which helps to clarify the Imo synthesis procedure.

1. Introduction

Imogolite (Imo) is a nanosized tubular clay mineral that mainly occurs in soils of volcanic origin (Levard and Basile-Doelsch, 2016) with an ideal structural formula being $(OH)_3Al_2O_3SiOH$. The structure model of Imo proposed by Cradwick et al. (1972) is commonly accepted and widely used in both experiments and theoretical calculations. According to this model, Imo is composed of a rolled gibbsite sheet with isolated orthosilicate groups (O_3SiOH) attached to the inside of the cylinders, each group bridging three oxygen atoms over the vacant octahedral site of the gibbsite sheet (Alvarez-Ramirez, 2007). The short Si—O bonds are the main factor which impart a strong curvature to the octahedral sheet, forming a tubular structure with Al—OH on the outside and Si—OH directing toward the center of the tube (Lee et al., 2011).

Generally, Imo has a length ranging from hundreds of nanometers to several micrometers, an inner diameter of about 1 nm and an outer diameter of approximately 2 nm. These dimensions differ from those of tubular halloysite (Hal), another nanosized tubular clay mineral with a unique meso/macroporous 1D channel (0.02–30 μm in length and 10–100 nm in inner diameter) (Yuan et al., 2008, 2015; Zhang et al., 2016). Compared with Hal, whose external surface consists of inert siloxane (Si—O—Si) groups, Imo has active hydroxyl groups on both the internal and external surfaces, which provides more possibilities for its modification (Bergaya et al., 2016; Bonelli, 2016). Moreover, Imo is the hydrophilic counterpart of carbon nanotube (CNT) that has attracted great interest over the past two decades (Amara et al., 2015). The unreactive nature of the CNT internal surface makes it hard to control its properties, limiting its use in “molecular recognition” applications that exploit its one-dimensional porosity (Kang et al., 2014). In contrast, the unique structure and special physical-chemical nature of Imo suggest it holds great promise for numerous applications, including clay polymer nanocomposites (Ma et al., 2011), liquid crystals (Paineau et al., 2016), chemical adsorption (Arai et al., 2006), catalysis (Imamura et al., 1993; Poli et al., 2016) and gas adsorption, separation and storage (Ackerman et al., 1993; Kang et al., 2014).

* Corresponding author at: CAS Key Laboratory of Mineralogy and Metallogeny/Guangdong Provincial Key Laboratory of Mineral Physics and Materials, Guangzhou Institute of Geochemistry, Chinese Academy of Sciences, 511 Kehua Street, Guangzhou 510640, China.
E-mail address: yuanpeng@gig.ac.cn (P. Yuan).

http://dx.doi.org/10.1016/j.clay.2017.09.021
Received 21 June 2017; Received in revised form 14 September 2017; Accepted 18 September 2017
Available online 23 September 2017

Unlike Hal, which has considerable global reserves, no commercial supply of Imo has thus far been reported. Natural high-grade Imo in Japan occurs as gel films over the surface of volcanoclastic rocks (Yoshinaga and Aomine, 1962). That sourced from soils requires a complicated purification process before its use, as it always coexists with allophane and other clay minerals (Yamamoto et al., 2007). Therefore till now, synthetic Imo rather than natural Imo is widely used in most studies of Imo (Bonelli, 2016). The first synthesized Imo was obtained by heating dilute solutions containing a hydroxyaluminosilicate complex (Farmer et al., 1977). Since then, many modifications on this protocol have been made for the sake of lowering the cost, improving the production or modifying the structure (Farmer and Fraser, 1979; Suzuki et al., 2000; Abidin et al., 2008).

However, only a few studies have focused on the time-dependent morphological and structural changes of Imo in the synthesis process, and many questions concerning the formation mechanism of the so-called proto-imogolite (proto-Imo) and its transition to Imo still remain to be resolved. This is possibly because direct observation of the morphology of Imo and proto-Imo is technically challenging due to their particles being very small and having a less-ordered and unstable structure. In fact, Imo and proto-Imo are quite fragile in interactions with electrons, which makes transmission electron microscopy (TEM) observation of their morphology be difficult. For example, in an earlier time-dependent study of normal Imo synthesis, only two typical TEM images obtained before and after a given reaction time (22.5 h) were given to show the changes in morphology of Imo (Wilson et al., 2001). However, direct microscopic observation of the full-range products, i.e., amorphous precursors, nanoscale intermediates (proto-Imo) and the final products, has rarely been achieved, although these products have been described on the basis of some simulation studies (González et al., 2014) and of spectroscopic studies (Mukherjee et al., 2007).

In this study, a combination of atomic force microscopy (AFM), X-ray diffraction (XRD), Fourier transform infrared (FTIR) spectroscopy, nuclear magnetic resonance (NMR) and N_2 physisorption techniques were used to monitor the time-dependent morphological, structural and textural changes of Imo and its intermediates during the synthesis process. The results of this work are useful for understanding the formation mechanism and structure of proto-Imo and Imo.

2. Experimental

2.1. Materials and Imo preparation

Orthosilicate sodium (Na_4SiO_4) was purchased from Nacalai Tesque, Japan. Aluminum chloride hexahydrate ($AlCl_3{\cdot}6H_2O$), sodium hydroxide (NaOH), hydrochloric acid (HCl) and ammonia ($NH_3{\cdot}H_2O$) were provided by Guangzhou Chemical Reagent Factory, China. All reagents were of analytical grade and used as received. Ultrapure water (18.25 MΩ·cm) was used in all experiments.

The synthesis of Imo followed a procedure previously reported (Ookawa et al., 2006). In a typical run, 100 mL of 0.15 M aluminum chloride solution and 100 mL of 0.10 M orthosilicate sodium solution were mixed under continuous stirring. 1 h later, 0.10 M NaOH solution was added to the obtained soluble hydroxyaluminosilicate solution at a rate of 0.5 mL/min until the pH reached 5.5. The as-received dispersion was centrifuged at 5000 rpm for 10 min. The supernatant was discarded and the transparent gel was washed with water and then redispersed in 2 L of water, into which 40 mL of 0.10 M hydrochloric acid was added with the aid of a magnetic stirrer. Acidified solutions obtained by repeating the aforementioned operations 10 times were heated and maintained at 98 °C for 1, 3, 6, 12, 18, 24, 48, 72, 96 and 120 h, respectively. After cooling to room temperature, aliquots (20 mL) were taken from each solution for AFM specimen preparation. The remaining parts were adjusted to a pH of 8 with 10 wt% ammonia to flocculate the products. Bulky gel, obtained by centrifuging the dispersions at 5000 rpm for 10 min, was dialyzed in water for 4 days and then freeze-dried. White powders or snow-like solids were obtained and labeled as Imo_{nh}, where n represented the duration in hours for which the precursors were maintained at 98 °C. Another precursor prepared following the same procedure but not heated to 98 °C was labeled as Imo_{0h}.

2.2. Characterization methods

AFM characterization was performed on a Bruker Multimode 8 scanning probe microscope with a silicon tip on a nitride lever. ScanAsyst-air mode was used for scanning Imo. To prepare the specimens, a mica sheet was cleaved (yielding a smooth negatively charged surface) and dipped into a dispersion of Imo for 30 s. Positive-charged Imo adsorbed onto the mica surface via electrostatic interaction. Then, two cleaning steps in water were performed to eliminate excess material. All of the specimens were dried in air for one week before AFM measurement. Based on the AFM results, the amount and length of Imo obtained at defined reaction times were measured and analyzed using Nano Measurer 1.2.

XRD analysis was performed on a Bruker D8 Advance diffractometer (Manheim, Germany) with a Ni filter and Cu Kα radiation (λ = 0.154 nm) generated at 40 kV and 40 mA. The specimens were investigated from 2° to 70° (2θ) with a step size of 0.02° and a measuring time of 0.8 s per step.

FTIR spectra were recorded using a Bruker Vertex 70 IR spectrometer (Manheim, Germany) at room temperature. The specimens were prepared by mixing 0.9 mg of sample and 80 mg of KBr followed by pressing the mixture into pellets. A pure KBr wafer was measured as the background. All of the spectra were collected over 64 scans in the range of 4000–400 cm^{-1} at a resolution of 4 cm^{-1}.

Solid state ^{29}Si cross-polarization magic-angle-spinning (CP/MAS) NMR and ^{27}Al MAS NMR was recorded using a Bruker AVANCE III 600 spectrometer in a static magnetic field of 14.1 T at a resonance frequency of 119.2 MHz and 156.4 MHz, respectively. ^{29}Si CP/MAS NMR experiments were recorded using a contact time of 5 ms, a recycle delay of 5 s, and a spinning rate of 10 kHz. ^{27}Al MAS NMR spectra were recorded on a 4 mm probe by small-flip angle technique with a pulse length of 0.5 μs (< π/12), a recycle delay of 1 s and a spinning rate of 14 kHz. The chemical shifts of ^{29}Si and ^{27}Al were referenced to TMS and 1 mol/L $Al(NO_3)_3$, respectively.

Nitrogen adsorption-desorption isotherms were measured on a Micromeritics ASAP 2020 system (Micromeritics Co. Norcross, USA) at liquid nitrogen temperature (− 196 °C). Before the measurement, the samples were outgassed at 250 °C for 12 h. The specific surface area (S_{BET}) value was calculated using the multiple-point Brunauer-Emmett-Teller (BET) method (Rouquerol et al., 2007), and the total pore volume (V_{total}) was evaluated from the N_2 uptake at a relative pressure of approximately 0.97 (Gregg and Sing, 1982). The t-plot method was used to calculate the microporous specific surface area (S_{micro}) and the micropore volume (V_{micro}). The pore size distributions (PSD), ranging from 0.45 to 10 nm, were analyzed using non-local density functional theory (NLDFT) (Thommes et al., 2015).

3. Results and discussion

3.1. Morphological and structural evolutions of the intermediates and final products

3.1.1. Formation and characteristics of the proto-imogolite (Imo_{0h})

In the XRD pattern of Imo_{0h} (Fig. 1a), three broad reflections centered at 6.8°, 27° and 40° (2θ) indicated its short-range ordered nature. The latter two reflections, with d-values of 0.33 and 0.225 nm, were ascribed to the 2D unit cell of Al—OH—Al (Lee et al., 2014) and were specific to allophane (Parfitt, 1990; Harsh et al., 2002). According to Thill et al. (2017), allophane exists as 4–5 nm hollow spheres with an imogolite local structure (ImoLS[1]), which represents a curved gibbsite

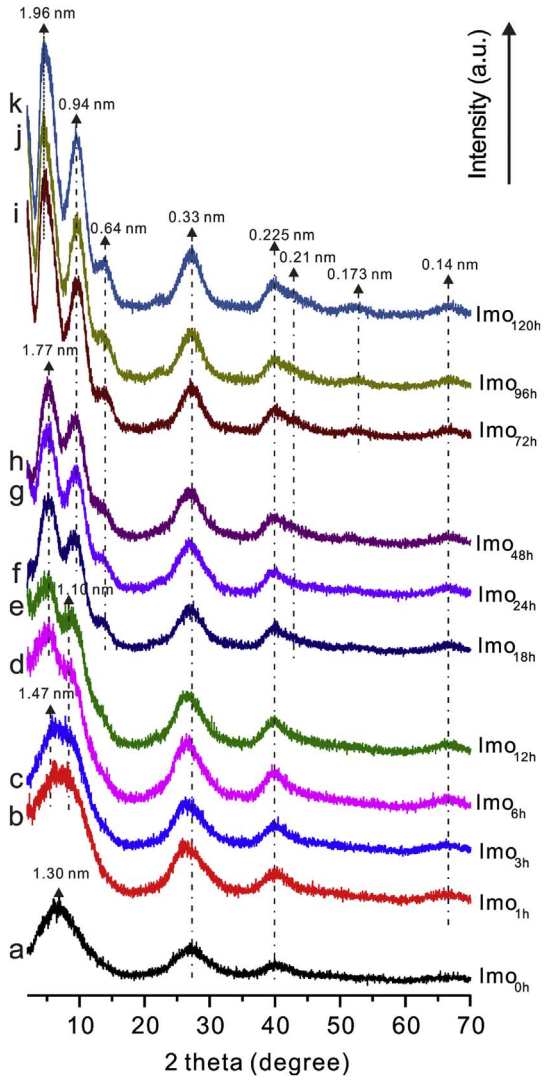

Fig. 1. XRD patterns of Imo obtained at defined reaction times.

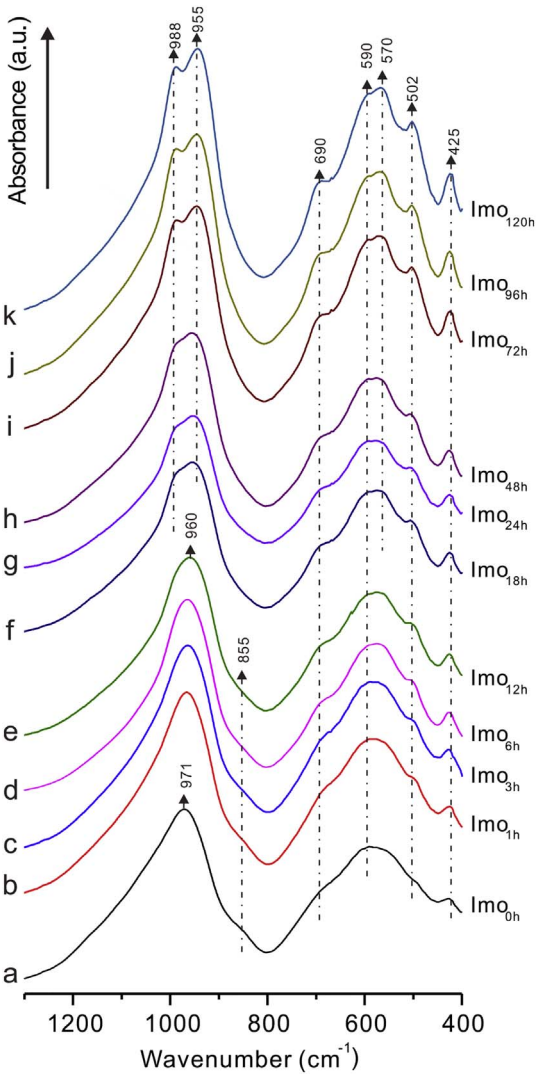

Fig. 2. FTIR spectra of Imo obtained at defined reaction times.

sheet with Si tetrahedral monomers linked to six Al octahedra inside the vacancies, so allophane and Imo could be taken as nanopolymorphs with ImoLS. Based on these results, an ImoLS was very likely to be formed in Imo_{0h}.

In the FTIR spectrum of Imo_{0h} (Fig. 2a), the presence of two bands at 502 and 425 cm^{-1}, related to Al—O—Al bending vibrations and various Al—O stretching vibrations (Wada and Wada, 1982) respectively, indicated an ImoLS had formed (Parfitt, 1990). In addition, a shoulder band at 855 cm^{-1}, attributed to OH deformation, also appeared in the FTIR of dehydrated allophane (Russell et al., 1969). Moreover, a single band near 1000 cm^{-1} ascribed to Si—O stretching vibration appeared in the FTIR spectrum of Imo_{0h} (Fig. 2a). This feature was used to distinguish allophane from Imo whose FTIR spectrum showed two bands at about 1000 cm^{-1} (Wada and Yoshinag, 1969; Wada, 1989). These results showed that the initial ImoLS formed in Imo_{0h} were not dominated by a tubular morphology. That is, Imo_{0h} was mainly composed of gibbsite-like fragments with Si—O tetrahedrons substituting hydroxyls on one side, which showed no preferred orientation in *a-b* plane of the gibbsite sheet.

An AFM image (with section profile) of Imo_{0h} was shown in Fig. 3a. Nanoparticles with z-scans of approximately 0.5–1.0 nm were found to be uniformly distributed on the mica sheet, summarized from repeated observations and section analysis. An area selected from the AFM image of Fig. 3a and reported with higher magnification in Fig. 3b showed two isolated particles with z-scans of 0.6 and 0.8 nm, respectively. Note that due to the convolution with probe tips, the heights obtained by section analysis rather than the horizontal distances measured in AFM images were generally used to estimate the dimensions of the samples. The AFM results indicated that the already-formed material with an ImoLS was fragments with an open structure in contrast with closed ImoLS (Imo or allophane). These open structures adsorbed flat on mica sheet and the z-scans essentially measured its wall thickness which was in the range 6–7 Å. In the following, the notion of open ImoLS is introduced to describe the early spherical or tubular ImoLS. In a study of the synthesis of Al—Ge Imo using ^{27}Al NMR, extended X-ray adsorption fine structure (EXAFS) spectroscopy at Ge—K edge and in situ small angle X-ray scattering (SAXS), Levard et al. (2010) found that open Imo tube pieces of about 5 nm formed at ambient temperature relatively quickly; the solids obtained before heating were found to be proto-Imo with 26% of Ge vacancies and varying curvatures. The AFM results of this study clearly supported this proposal.

In the ^{29}Si CP/MAS NMR spectrum of Imo_{0h}, two resonances were observed (Fig. 4a). An intense resonance at a chemical shift of − 78 ppm was assigned to the well-defined $Q^3(6Al)$ coordination, where a silanol group was connected through oxygen with six octahedral Al atoms (Kang et al., 2010; Yucelen et al., 2012a). Such Si

[1] ImoLS is used instead of the previously introduced notation ILS to be in agreement with the recommended abbreviation for Imogolite.

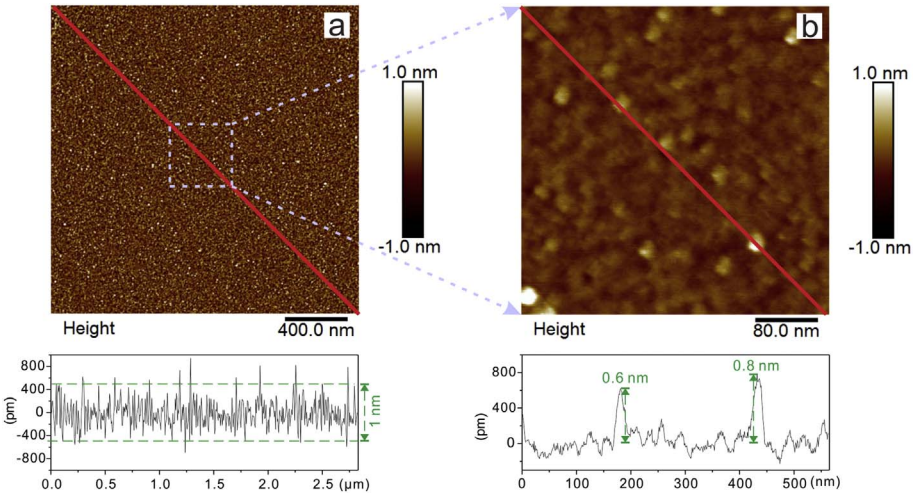

Fig. 3. AFM images and section profiles of Imo_{0h}: a, distribution of Imo_{0h} on mica sheet and its overall size (smaller than 1 nm); b, local magnification of a, showing the exact sizes of two isolated particles being 0.6 and 0.8 nm.

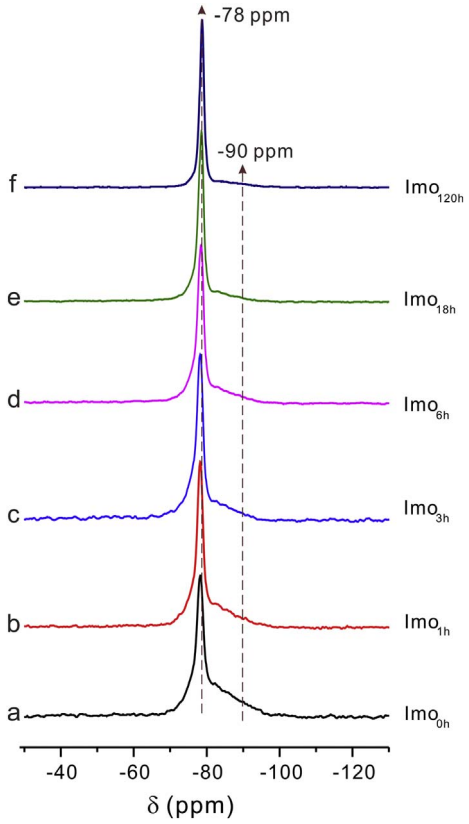

Fig. 4. ^{29}Si CP/MAS NMR spectra of Imo obtained at defined reaction times.

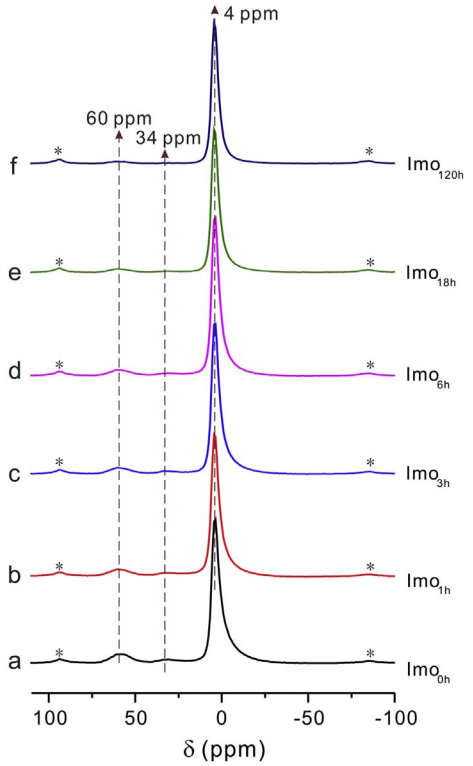

Fig. 5. ^{27}Al MAS NMR spectra of Imo obtained at defined reaction times. The asterisks (*) denote the spinning side bands.

coordination was widely reported for Imo and used in its detection (Barron et al., 1982). But according to Hiradate and Wada (2005), this resonance was also typical for allophane. So this resonance was more likely to be ascribed to open/closed ImoLS (both spherical and tubular) than to only Imo. The other weak and broad resonance centered at approximately −90 ppm, was also observed for allophane (Hiradate and Wada, 2005), and it was attributed to a small but significant fraction of less ordered Si species with 0–5 next-nearest neighbor Al atoms (Yucelen et al., 2011). The ^{29}Si NMR results of Imo_{0h} indicated the ImoLS dominated the products.

A main resonance at 4 ppm was shown in the ^{27}Al MAS NMR spectrum of Imo_{0h} (Fig. 5a). The resonance indicated the presence of octahedral Al atom (Al^{VI}), which came from the structure units of gibbsite-like sheet and represented the major part of ImoLS (Yucelen et al., 2011). This chemical shift corresponded to the Al coordination in Imo and allophane (Hiradate and Wada, 2005). This spectrum also showed a signal at 60 ppm, which was ascribed to Al^{IV} and corresponded to a transient phase formed in variable amounts during Imo synthesis (Yucelen et al., 2011). Besides these two commonly reported peaks, another small peak at about 34 ppm appeared. This resonance was likely to be assigned to Al^{V}, which occurred in allophane whose structure was poor in octahedra relative to tetrahedra (Childs et al., 1999).

All these results, from the aspects of local structure, morphology and molecular coordination, indicated that open ImoLS was the dominant phase in Imo_{0h}. The obtained open ImoLS presumably had a spherical or tubular curvature depending on their sizes.

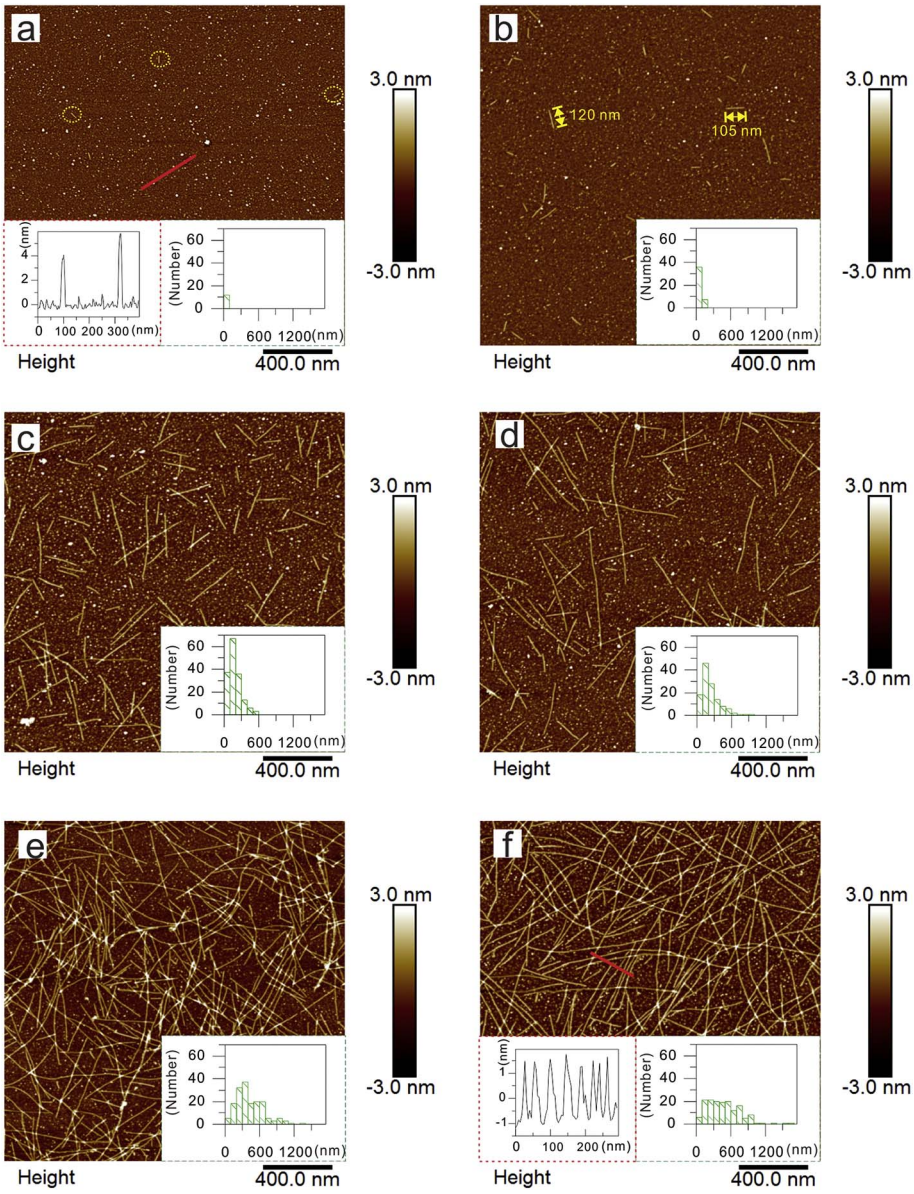

Fig. 6. AFM images of a, Imo_{1h}; b, Imo_{3h}; c, Imo_{12h}; d, Imo_{24h}; e, Imo_{72h} and f, Imo_{120h}. Insets on the bottom right (a–f) are length distribution histograms; insets on the bottom left (a, f) show the sizes of allophane (4–6 nm) and Imo (2.2 ± 0.2 nm) by section analysis.

3.1.2. Growth and internal reconstruction of proto-Imo (from Imo_{1h} to Imo_{12h})

The AFM image of Imo_{1h} was shown in Fig. 6a. A few nanoparticles with z-scans of 4–6 nm and large quantities of small objects with z-scans of less than 1 nm or about 2 nm, together with several tubes with z-scans of about 2 nm, were found to be distributed on the mica sheet. This result was summarized from repeated observations and section analysis. Note here that the observed nanoparticles on mica sheet were collected through an adsorption mechanism which might induce some artifacts in their relative proportions due to their different charges and diffusion coefficients. It was thus not straightforward to use AFM for quantitative interpretation of the relative concentrations of particles with different lengths and shapes. As shown in the inset on the bottom left of Fig. 6a, two isolated particles had sizes of 4 and 6 nm, respectively. The sizes of these nanoparticles were consistent with the size of allophane (Parfitt, 1990; Thill et al., 2017), which indicated that these nanoparticles were likely to be allophane. The particles with z-scans less than 1 nm were open ImoLS adsorbed flat on mica as discussed above and particles about 2 nm was likely to be very short Imo. These AFM results clearly showed the very first 'closed' ImoLS had formed in Imo_{1h}. Indeed, the open ImoLS adsorbed flat on the mica (1 nm or less in z-scans) but once closed in the shape of a sphere or a tube, they appeared as z = 2 nm tubes (Imo) or z = 4–6 nm spheres (allophane). The fact that both spherical and tubular closed ImoLS form at this early stage tend to show that the size distribution of the open ImoLS spans over the sphere/tube transition described by Thill et al. (2017).

In the XRD pattern of Imo_{1h} (Fig. 1b), the reflection at 6.8° (1.30 nm), corresponding to some long-range ordering according to Wada (1989), resolved into two overlapping reflections at 6° (1.47 nm) and 8° (1.10 nm). This result indicated that the overall structure of the solid products was becoming more ordered. In other words, the open ImoLS was growing. If this was the case, more and more open ImoLS would experience a sphere/tube transition and the formation of allophane-like closed ImoLS would be less and less probable as the reaction proceeded. Imo with a tubular closed ImoLS probably formed via edge-edge aggregation of proto-Imo with a tubular open ImoLS or by their attachment to the active end of already-formed Imo as reported by Yucelen et al. (2013). In the XRD pattern of Imo_{6h}, the reflections evolved further into two separated ones and the first one shifted to 5° (1.77 nm), suggesting the formation of a relatively high amount of materials with tubular open/closed ImoLS.

In ^{29}Si CP/MAS NMR spectra (Fig. 4a–d), the relative intensity of

the resonance centered at approximately −90 ppm decreased a lot in the first 6 h. This indicated that amorphous or less-ordered materials (maybe spherical open ImoLS with a smaller size) were growing and becoming more ordered (maybe tubular open ImoLS with a bigger size). According to the Al liquid-state NMR results carried out by Yucelen et al. (2011), the species with an ImoLS does not increase to a significant extent as a function of time, and the decrease in relative intensity of this broad resonance was a result of ordering of Al atoms that already in an ImoLS with Si species [Si(*n*Al) → Si(6Al)]. In agreement with this change, significant decreases in relative intensity of the signals at 60 and 34 ppm in the ^{27}Al NMR were observed in the first 6 h (Fig. 5a–d), suggesting the transformation of disordered Al environments to ordered nanotube-like configurations.

As the synthesis reaction proceeded, the vibration band at 855 cm^{-1} in the FTIR spectra mentioned previously declined and almost disappeared in Imo_{12h} (Fig. 2a–e). This band could be interpreted as a signature of a spherical open ImoLS. Meanwhile, the band at 690 cm^{-1}, which was attributed to O—Al—O vibrations and characteristic of a tubular open/closed ImoLS (Levard et al., 2012), evolved from a small and less-resolved shoulder band into a well-defined band in Imo_{6h} (Fig. 2e), indicating the formation of products with a tubular open/closed ImoLS. All these observations confirmed the transformation from a spherical open ImoLS to a tubular open ImoLS. In addition, the broad band near 590 cm^{-1} in Imo_{0h} gradually evolved into two overlapping bands at 590 and 570 cm^{-1}. The former, ascribed to the stretching vibration of Si—O—Al, existed in the structure of proto-Imo (Arancibia-Miranda et al., 2011). The latter, assigned to the Al octahedra, arose from an octahedral sheet similar to the gibbsite sheet present in Imo (Levard et al., 2012). Their band intensity ratio (570 cm^{-1}/590 cm^{-1}) kept increasing as the reaction proceeded, showing a further evolution from proto-Imo with a tubular open ImoLS to Imo with a tubular closed ImoLS. In fact, several Imo particles with lengths of dozens of nanometers could be identified with certainty in the AFM images of Imo_{1h} (Fig. 6a). Some Imo particles with lengths of more than 100 nm appeared in Imo_{3h} (Fig. 6b), although the majority were shorter than 100 nm, as shown in the inset of Fig. 6b. The amount of both proto-Imo and Imo kept increasing, as illustrated by the AFM results shown in Fig. 6a–c and S1a, at least for the first 12 h of reaction time.

All these preceding results showed that proto-Imo with an open ImoLS grew and aggregated into either tubular or spherical closed ImoLS. Only a precise monitoring of the shape of the newly formed closed ImoLS when the temperature rose could enable a complete understanding of the potential sphere/tube shape transition and coexistence. González et al. (2014) found by molecular dynamics calculations that the open ImoLS adopted shapes mainly depended on temperature. But due to periodic boundary conditions used in those simulations, only tubular structures were explored. Further research adapted to the lake of symmetry of the open ImoLS should be tried in the future. This might constitute experimental evidence for the hypothesis, proposed by Thill et al. (2017), that a spherical to tubular shape transition occurred as the size of proto-Imo increased.

3.1.3. Characteristics of assembly of Imo via consumption of proto-Imo (Imo_{18h}–Imo_{48h})

In the FTIR spectrum of Imo_{18h} (Fig. 2f), the presence of two bands near 1000 cm^{-1}, i.e., at 988 and 955 cm^{-1}, were ascribed to Si—O stretching vibrations. This feature was characteristic of tubular Imo (Cradwick et al., 1972). In addition, the overlapping bands at 590 and 570 cm^{-1} mentioned previously evolved further into two well-defined bands. This feature, which had not been reported previously, could also be characteristic of tubular Imo. Moreover, pronounced changes could be seen in the XRD pattern of Imo_{18h} (Fig. 1f). The presence of the reflections at 13.9° (0.64 nm) and 52.9° (0.173 nm) made the XRD profile of Imo_{18h} similar to that of the final products, although some reflections were less well-defined. In the ^{29}Si NMR spectrum of Imo_{18h} (Fig. 4e), the relative intensity of the resonance centered at about −90 ppm deceased and only a very small peak remained. Similar decrease happened for the resonances at 60 and 34 ppm in ^{27}Al NMR spectra (Fig. 5e). These findings demonstrated that Imo had already dominated the solid products in Imo_{18h}.

There were limited changes in the AFM results of Imo_{24h} compared with those of Imo_{18h} and Imo_{48h}. As shown in the inset of Fig. 6d, most of the Imo particles had lengths of 0–0.6 μm, and those with lengths of 100–200 nm were prevailing in Imo_{24h}. During this period, the size of proto-Imo probably reached a value beyond which tubular open ImoLS dominated. Although the point at which this happened could not be determined precisely due to the limited capability of AFM to distinguish proto-Imo with a spherical/tubular open ImoLS and even very short Imo (Figs. 6d and S1b,c). Meanwhile, the rate of Imo formation remained high with the accumulation of proto-Imo with a tubular open ImoLS. Again, the rate of allophane formation could be the key to detect the transformation from a spherical to a tubular open ImoLS.

3.1.4. Characteristics of well-formed Imo (from Imo_{72h} to Imo_{120h})

As shown in the AFM image of Imo_{72h} (Fig. 6e), particles with z-scans of less than 1 nm almost disappeared, and some particles with z-scans of ca. 2 nm (very short Imo) still existed, together with many well-dispersed individual nanotubes of various lengths, as they did in Imo_{96h} (Fig. S1d) and Imo_{120h} (Fig. 6f). These results indicated that proto-Imo with an open ImoLS was mostly consumed in assembling Imo, and the solids obtained mainly contain Imo, and maybe a few allophane. Three days could be the shortest possible time for completing the synthesis of Imo. In addition, as illustrated by the section profile shown in the inset on the bottom left of Fig. 4f, the synthetic Imo had a constant external diameter of 2.2 ± 0.2 nm. This value was in good agreement with the diameter (2.4 ± 0.2 nm) of Imo synthesized in HCl as measured directly by cryo-TEM (Yucelen et al., 2012b).

Moreover, both the XRD and FTIR results showed little changes after 72 h (Fig. 1i–k, 2i–k), which supported the assertion that 72 h could be the shortest duration needed for Imo formation by this synthesis route. The XRD pattern of Imo_{72h} resembled those of both natural and synthetic Imo (Donkai et al., 1992; Ohashi et al., 2004). The respective (006), (004) and (002) reflections at 66.8° (0.14 nm), 43° (0.21 nm) and 21° (0.42 nm) arose from a repeat distance (0.84 nm) along the tube axis previously obtained by electron diffraction analysis (Cradwick et al., 1972). According to Mukherjee et al. (2005), absence of the odd reflections along the *c* axis, e.g., (005) and (003), supported the cylindrical symmetry of Imo, and thus the (006), (004) and (002) reflections could be used to discriminate nanotubes from amorphous materials and other crystalline structures. The reflections at 4.5° (1.96 nm) and 9.3° (0.94 nm), which had the highest intensity, were due to the tubular shape of Imo (Thill, 2016). In this low angle region below 20°, many factors might affect the XRD pattern of Imo, such as external diameter, circumference, alignment and stacking, separation distance and axial dimensions (Harsh, 2012). Therefore the differences in the XRD patterns might result from different synthesis conditions and methods of sample preparation (dialysis and drying procedures). Kang et al. (2010, 2012) performed an explicit atomic-scale simulation of scattering from finite-size bundles to predict the XRD patterns. Based on the simulation results, these authors pointed out that the Imo particles in their study were not individually dispersed but formed small 2 × 2 or triangular bundles. However, compared with their simulation results (Kang et al., 2012), the Imo particles synthesized in this study were likely to be individually dispersed thanks to the freeze-drying procedure. In the FTIR spectra (Fig. 2a–h), the bands at 502 and 425 cm^{-1}, related to the ImoLS (Levard et al., 2012), became more intense as the reaction proceeded but remained unchanged since Imo_{72h} (Fig. 2i–k). All these previous results indicated that Imo was almost the only solid product after 72 h.

However, as shown by the length distribution histograms in Fig. 6, the average length of Imo kept increasing throughout the whole

reaction, even from Imo_{72h} to Imo_{120h}. This demonstrated that the already-formed Imo particles were still assembling into longer particles via oriented aggregation, which is now recognized as an important mechanism of crystal growth in synthetic, biogenic, and geologic environments (De Yoreo et al., 2015). The tip-tip collision mechanism proposed by Maillet et al. (2011) was essentially oriented aggregation; it required not only a collision between two nanotubes, but also a relative rotation until a thermodynamically favorable configuration was achieved (Li et al., 2012; Yucelen et al., 2013). Thill et al. (2017) further pointed out that Imo was an oriented nanotube. An Imo nanotube is not identical upon a 180° rotation. Therefore, tip-tip collisions also requires the two tubes to have the same orientation.

In the ^{29}Si NMR of Imo_{120h} (Fig. 4e), the small shoulder resonance at about −90 ppm still remained, which suggested the presence of less-ordered Si environments even in the final products that was expected to be pure Imo. A possible explanation was that it was also a part of the nanotube structure, and presented a distribution of the spectral parameters due to different orientations, bundling or bending of the nanotubes (Yucelen et al., 2012b). The small but definite residue of tetrahedral site at 60 ppm in the ^{27}Al NMR of Imo_{120h} (Fig. 4e) represented the "disordered" Al sites of the nanotube material, such as aluminum sites at the end of the nanotubes (Yucelen et al., 2011) or the structural defects in the Imo walls (Yucelen et al., 2012a).

3.2. Specific surface area and porosity changes during the synthesis process

Nitrogen physisorption reveals more textural information than AFM that focuses on a limited observation zone and may suffer from adsorption artifacts due to the quickest adsorption of the smallest objects. The N_2 adsorption/desorption isotherms and PSD curves of the Imo obtained at different reaction times were shown in Fig. 7. The isotherms of Imo_{0h} and Imo_{1h} (Fig. 7b) belonged to type II according to the IUPAC classification (Thommes et al., 2015), and their PSD results appeared as almost straight lines parallelling to the lateral axis (Fig. 7c,d). These results demonstrated that Imo_{0h} and Imo_{1h} had a nonporous nature. In addition, both of their S_{BET} values were very low (4.7 and 4.4 m^2/g, Table 1). A possible explanation why the nanoparticles shown in the AFM images (Figs. 3 and 6a) had such low S_{BET} values and nonporous nature was that they were less-ordered and aggregated heavily in the process of freeze-drying to lower their surface energy. Moreover, the open nature of the ImoLS at this stage does not allow any porosity to be built in the solid.

As shown in Fig. 7a, the isotherm of Imo_{12h} was classified as type I (a), which was characteristic of micropores. For Imo_{18h}, the isotherms turned into type I (b) with a limited hysteresis loop, a feature indictive of a wide range of pores from micropores to mesopores, most probably stemming from slit mesopores among bundles (Bonelli et al., 2009). As the reaction proceeded, the multilayer sections of the isotherms became steeper, indicating their external specific surface area ($S_{external}$) increased, an observation further supported by the data presented in Table 1. Indeed, the $S_{external}$ kept increasing throughout the reaction and reached 73.1 m^2/g in Imo_{120h}. A family of nanopores with diameters in the range of 0.5–10 nm were present (Fig. 7c,d), the largest population being those with a peak at 0.63 nm. This could be ascribed to the intrinsic nanotubular structure of Imo, i.e., pore A as reported by Ackerman et al. (1993), the size of which was in good agreement with the size (0.65–0.7 nm) of pore A previously obtained by N_2 adsorption analysis for the synthetic Imo (Ackerman et al., 1993; Mukherjee et al., 2005) and the inner diameter (0.64 nm) of Imo in theoretical studies (Cradwick et al., 1972; Brown et al., 1978; Brigatti et al., 2006). Concerning pore B with a theoretical diameter of 0.3–0.4 nm formed by three aligned Imo particles, N_2 adsorption technique might fail in characterizing them due to the steric effects (the diameter of N_2 molecule is 0.36 nm) (Thommes et al., 2015). Moreover, a freeze-drying method was employed in this study, with which the formation of pore B was limited. The small peaks at 1.02, 1.30 and 1.80 nm could be ascribed to the secondary pores of Imo (i.e., pore C) or a more complex pore structure formed by the connection of particles/aggregates. The discrepancy of pore C between this study and previous reports (e.g., Ackerman et al., 1993) might result from different arrangements of Imo in a filtrated powder or in a freeze-dried one. All of these values increased as the reaction went on.

3.3. Process and mechanism of Imo synthesis and growth

Based on the overall structure of the obtained solid products and the occurring main reactions, Imo synthesis process was described in five steps: i) formation of amorphous precursors by hydrolysis and condensation of Al and Si; ii) formation of proto-Imo with an open ImoLS at the expense of amorphous precursors; iii) open ImoLS dominates and through growth and internal reconstruction of proto-Imo gives either spherical or tubular closed ImoLS; iv) closed ImoLS dominates and open ImoLS are enlarged leading essentially to the formation of Imo with a closed tubular ImoLS by the consumption of the remaining proto-Imo with an open ImoLS; and v) no open ImoLS remains, and the reaction continues through the further growth of already-formed Imo via oriented aggregation. The overall mechanism of Imo synthesis and growth is described as follows and the five steps are schematically represented in Fig. 8.

- In step i), amorphous precursors form by hydrolysis and condensation of Al and Si in a diluted acidic solution. This step is believed to be very fast and almost finished even before Imo_{0h}. A synchrotron run for SAXS at Soleil in France carried out recently tends to confirm this vision (data is not yet published). The initial amorphous materials extend on very large sizes and quickly transform back into smaller objects. This process occurs in minutes.
- In step ii), from the amorphous material, proto-Imo having an open ImoLS quickly form as the Si tetrahedrons attached to gibbsite sheets makes them to curl. The size distribution of the open ImoLS with respect to the size threshold for a sphere/tube shape transition (Thill et al., 2017) may be a key point for the control of the proportion of the spherical or tubular closed ImoLS. In natural systems, the widely observed coexistence of allophane and Imo in various proportions is probably controlled at this step. The open ImoLS tends to aggregate heavily in the drying process due to its high surface energy, which results in its extremely low S_{BET} and nonporous nature.
- In step iii), proto-Imo is the dominating product. The average size of the proto-Imo with an open ImoLS probably increases once the dispersions are heated in the synthesis process. Once formed, proto-Imo particles with an open ImoLS assemble into either spheres (allophane) or tubes (Imo) depending on their sizes. Meanwhile, the short Imo particles assemble into long Imo particles via oriented aggregation. At an early stage (e.g., the first 12 h of reaction time), the transformation of proto-Imo into Imo simultaneously occur, resulting in an increase of the pore volume of the dry powder.
- In step iv), closed ImoLS dominate with proto-Imo largely consumed. As the tubular closed ImoLS represents the majority of the shape, the typical IR doublet is clearly noticed at this stage. The synthesis of Imo slows over time as the proto-Imo with an open ImoLS is consumed. Heating is required not only for the open ImoLS to close in the formation of tubes or spheres, but also for the tubes to grow since this part of the process is particularly slow at ambient temperature.
- In step v), at about 72 h, proto-Imo with an open ImoLS is almost used up. The obtained solids mainly contain Imo, and maybe a few of allophane particles. Allophane, once formed, is not likely to transform into Imo in such a synthesis system. At this step, the length of already-formed Imo particles increases further by oriented aggregation. The growth kinetic, however, considerably slows as the average length $< l >$ of the nanotube increase because the

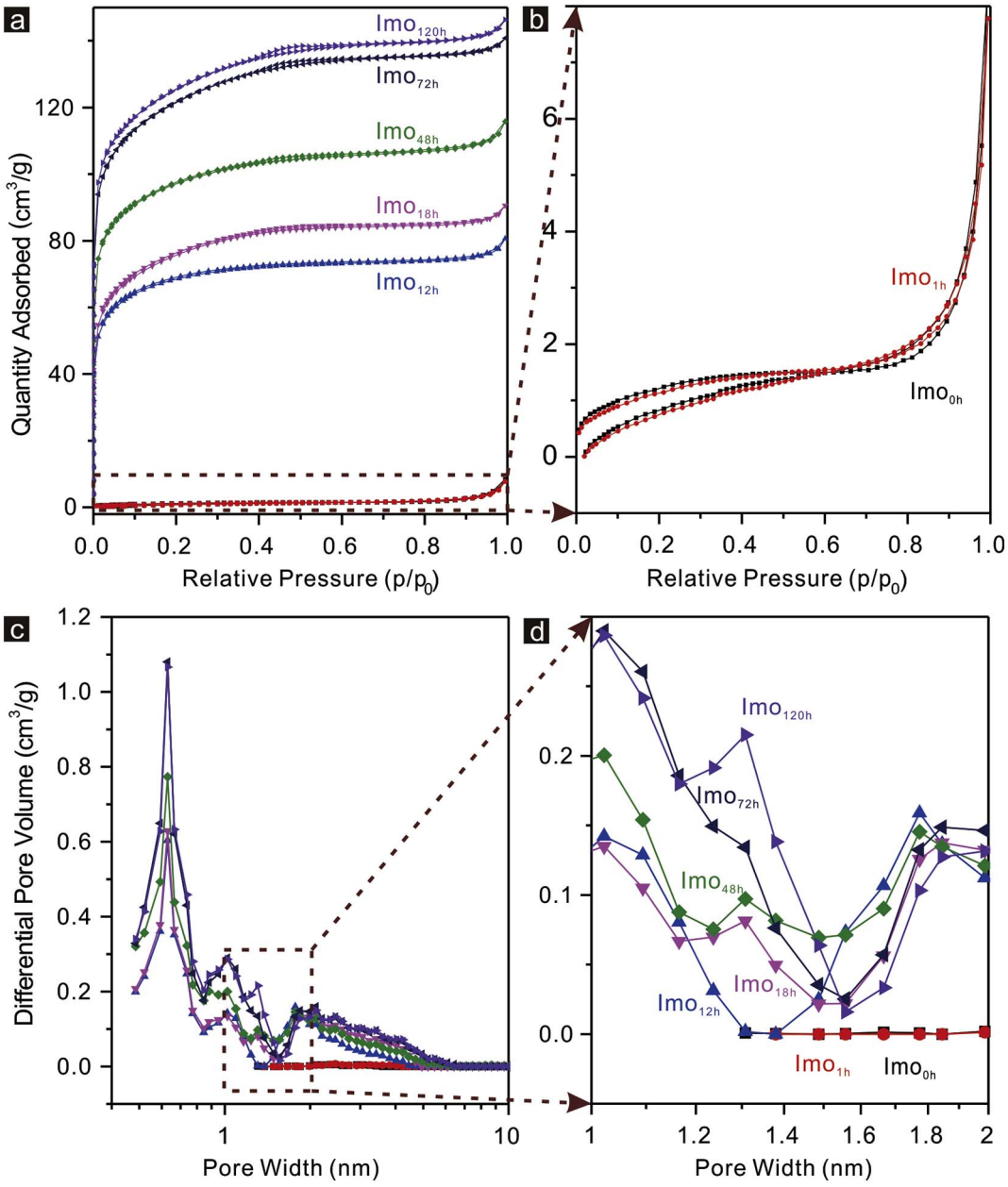

Fig. 7. Nitrogen adsorption/desorption isotherms (a, b) and pore size distributions (c, d) of Imo obtained at different reaction times; b and d are magnifications of the dotted rectangles in a and c, respectively.

Table 1
Textural data calculated from N_2 adsorption/desorption analysis.

	S_{BET} (m^2/g)	S_{micro} (m^2/g)	$S_{external}$ [a] (m^2/g)	V_{total} (cm^3/g)	V_{micro} (cm^3/g)
Imo_{0h}	4.7	3.2	1.5	0.0085	0.0013
Imo_{1h}	4.4	2.1	2.3	0.0008	0.0007
Imo_{12h}	256.4	231.0	25.4	0.1199	0.0948
Imo_{18h}	273.4	228.0	45.4	0.1361	0.0971
Imo_{48h}	360.4	314.2	46.2	0.1733	0.1294
Imo_{72h}	449.7	379.1	70.6	0.2144	0.1559
Imo_{120h}	458.9	385.8	73.1	0.2221	0.1607

[a] $S_{external} = S_{BET} - S_{micro}$.

aggregation rate is proportional to $< l >^{-4}$ (Maillet et al., 2010).

3.4. Implication to the Imo formation in natural systems

Imo and allophane widely occur in natural silica-rich environments where sufficient moisture for leaching of silica exists (Levard and Basile-Doelsch, 2016), but their intermediates (i.e., proto-Imo and proto-allophane) are rarely reported. Few studies have mentioned about proto-allophane, since the allophane formation mechanism is not well understood. The results obtained in this study provide some ideas about how open ImoLS forms in natural environment. In humid climates, the weathered volcanic glass dissolves, giving rise to Al^{IV} and monosilicic acid (Hiradate and Wada, 2005). The obtained Al^{IV} transforms into Al^{VI} and then hydrolyzes, forming gibbsite-like sheets. Open ImoLS forms via the reaction between the gibbsite-like sheets and the monosilicic acid. Depending on its size, the open ImoLS can be either spherical or tubular. This is a temporary step that leads to the formation

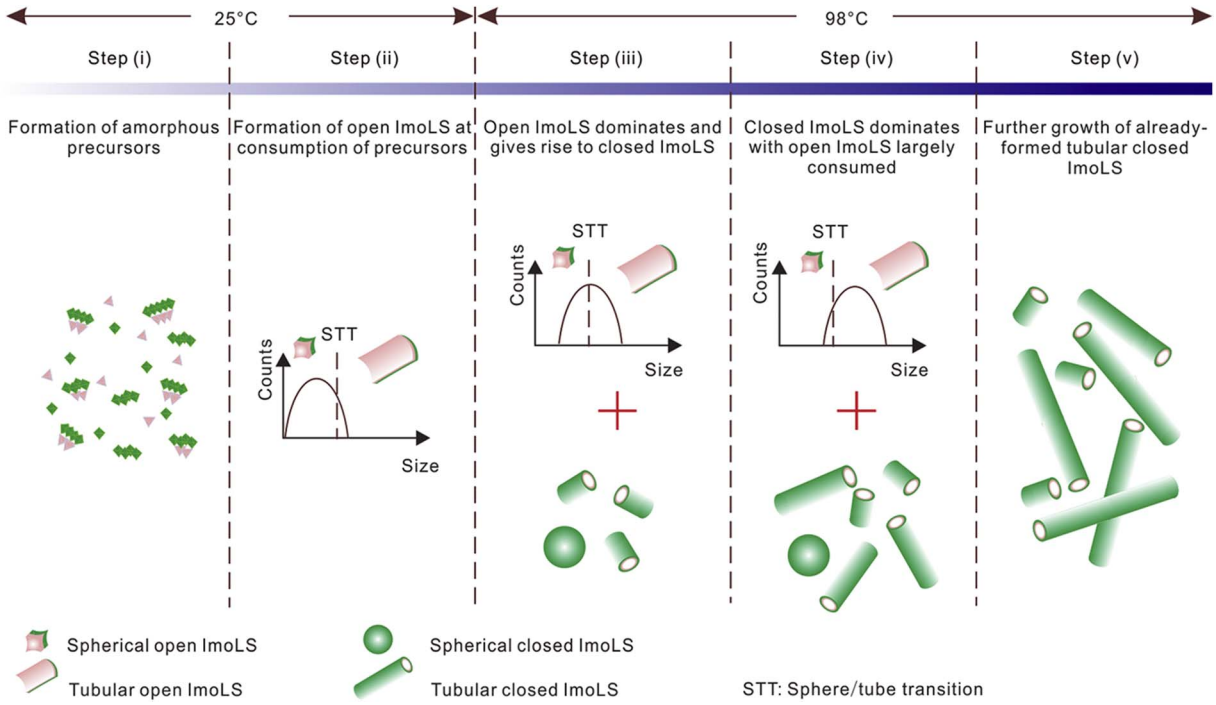

Fig. 8. Five steps in sol-gel growth of Imo.

of Imo/allophane, which might control the proportions of Imo and allophane in soils. It occurs in solutions as well as on the surface of volcanic glass. The obtained open ImoLS has a similar (if not identical) structure as hydroxyaluminosilicates (HAS_A) synthesized by Doucet et al. (2001). If the monosilicic acid is present in excess, it will react with HAS_A to form another kind of hydroxyaluminosilicates (HAS_B). Both HAS_A (maybe proto-Imo/proto-allophane) and HAS_B (maybe precursors of kaolinite or halloysite) are representative of HAS found in soil horizons. They are extremely insoluble (Doucet et al., 2001) and have nearly amorphous nature and small sizes in nanometer and sub-nanometer range, which makes it difficult to identify them in soils. These features imply that they might widely occur throughout the surface environments of the earth. However, as mentioned above, no Imo ores with economic potential have been discovered up to now. A possible reason for this is that the transformation from proto-Imo/proto-allophane to Imo/allophane requires strict conditions. Many factors, e.g., the activity of Si in soil solution, the availability of Al species, the opportunity for co-precipitation, soil organic compounds and pH, will lower the chances of large-scale formation of Imo or allophane (Parfitt, 2009).

4. Conclusions

The time-dependent changes in morphology and structure of the intermediates and final products during the sol-gel growth of Imo were observed via a combination of characterizations including AFM, XRD, FTIR, NMR and N_2 physisorption. The main stages of Imo growth were classified based on the structural changes of the solid products at each stage. At the beginning of the reaction, the amorphous precursors obtained by hydrolysis and condensation of Al and Si were quickly consumed, and proto-Imo with an open ImoLS and z-scans of less than 1 nm was formed. This initial proto-Imo had a broad size distribution that spanned over the sphere/tube transition threshold, implying that the open ImoLS could be either spherical or tubular. Most of the proto-Imo with a spherical open ImoLS grew further and transformed into proto-Imo with a tubular open ImoLS via internal reconstruction, during which time the temperature played a key role on the sphere/tube shape transition. The as-received proto-Imo with a tubular open ImoLS was consumed in the assembling of Imo with a tubular closed ImoLS. A small amount of proto-Imo with a spherical open ImoLS condensed with each other to give rise to allophane with a spherical closed ImoLS. As the proto-Imo with a spherical/tubular open ImoLS was largely consumed, the overall reaction slowed down. The already-formed Imo particles continued to assemble and form longer Imo particles via oriented aggregation. These findings provide some fundamental data to clarify the Imo synthesis procedure, and some insights into the formation mechanism of allophane and Imo in natural environments.

Acknowledgements

Financial supports from the National Natural Scientific Foundation of China (Grant No. 41472045 and 41672042) and Youth Innovation Promotion Association CAS and CAS/SAFEA International Partnership Program for Creative Research Teams (Grant No. 20140491534) are gratefully acknowledged. This is a contribution (No. IS-2437) from GIGCAS.

Appendix A. Supplementary data

Supplementary data to this article can be found online at http://dx.doi.org/10.1016/j.clay.2017.09.021.

References

Abidin, Z., Matsue, N., Henmi, T., 2008. A new method for nano tube imogolite synthesis. Jpn. J. Appl. Phys. 47, 5079–5082.
Ackerman, W.C., Smith, D.M., Huling, J.C., Kim, Y.W., Bailey, J.K., Brinker, C.J., 1993. Gas/vapor adsorption in imogolite: a microporous tubular aluminosilicate. Langmuir 9, 1051–1057.
Alvarez-Ramirez, F., 2007. Ab initio simulation of the structural and electronic properties of aluminosilicate and aluminogermanate natotubes with imogolite-like structure. Phys. Rev. B 76, 125421.
Amara, M.S., Paineau, E., Rouzière, S., Guiose, B., Krapf, M.-E.M., Taché, O., Launois, P., Thill, A., 2015. Hybrid tunable-diameter metal-oxide nanotubes for organic molecules trapping. Chem. Mater. 27, 1488–1494.
Arai, Y., McBeath, M., Bargar, J., Joye, J., Davis, J., 2006. Uranyl adsorption and surface speciation at the imogolite-water interface: self-consistent spectroscopic and surface complexation models. Geochim. Cosmochim. Acta 70, 2492–2509.
Arancibia-Miranda, N., Escudey, M., Molina, M., Garcia-Gonzalez, M.T., 2011. Use of

isoelectric point and pH to evaluate the synthesis of a nanotubular aluminosilicate. J. Non-Cryst. Solids 357, 1750–1756.
Barron, P.F., Wilson, M.A., Campbell, A.S., Frost, R.L., 1982. Detection of imogolite in soils using solid-state Si-29 NMR. Nature 299, 616–618.
Bergaya, F., Thill, A., Yuan, P., 2016. Epilogue. In: Yuan, P., Thill, A., Bergaya, F. (Eds.), Nanosized Tubular Clay Minerals. Elsevier, Amsterdam, pp. 735–738.
Bonelli, B., 2016. Surface chemical modification of imogolite. In: Yuan, P., Thill, A., Bergaya, F. (Eds.), Nanosized Tubular Clay Minerals. Elsevier, Amsterdam, pp. 279–307.
Bonelli, B., Bottero, I., Ballarini, N., Passeri, S., Cavani, F., Garrone, E., 2009. IR spectroscopic and catalytic characterization of the acidity of imogolite-based systems. J. Catal. 264, 15–30.
Brigatti, M.F., Galan, E., Theng, B.K.G., 2006. Structures and mineralogy of clay minerals. In: Bergaya, F., Theng, B.K.G., Lagaly, G. (Eds.), Handbook of Clay Science. Elsevier, Amsterdam, pp. 19–86.
Brown, G., Newman, A.C.D., Rayner, J.H., Weir, A.H., 1978. The structures and chemistry of soil clay minerals. In: Greenland, D.J., Hayes, M.H.B. (Eds.), The Chemistry of Soil Constituents. Wiley, Chichester, pp. 29–178.
Childs, C.W., Hayashi, S., Newman, R.H., 1999. Five-coordinate aluminum in allophane. Clay Clay Miner. 47, 64–69.
Cradwick, P.D., Wada, K., Russell, J.D., Yoshinag, N., Masson, C.R., Farmer, V.C., 1972. Imogolite, a hydrated aluminum silicate of tubular structure. Nat. Phys. Sci. 240, 187–189.
De Yoreo, J.J., Gilbert, P.U., Sommerdijk, N.A., Penn, R.L., Whitelam, S., Joester, D., Zhang, H., Rimer, J.D., Navrotsky, A., Banfield, J.F., 2015. Crystallization by particle attachment in synthetic, biogenic, and geologic environments. Science 349, aaa6760.
Donkai, N., Miyamoto, T., Kokubo, T., Tanei, H., 1992. Preparation of transparent mullite-silica film by heat-treatment of imogolite. J. Mater. Sci. 27, 6193–6196.
Doucet, F.J., Schneider, C., Bones, S.J., Kretchmer, A., Moss, I., Tekely, P., Exley, C., 2001. The formation of hydroxyaluminosilicates of geochemical and biological significance. Geochim. Cosmochim. Acta 65, 2461–2467.
Farmer, V.C., Fraser, A.R., 1979. Synthetic imogolite, a tubular hydroxyaluminium silicate. In: Mortland, M.M., Farmer, V.C. (Eds.), Proceedings of the 5th International Clay Conference, Oxford, 1978. Elsevier, Amsterdam, pp. 547–553.
Farmer, V.C., Fraser, A.R., Tait, J.M., 1977. Synthesis of imogolite: a tubular aluminum silicate polymer. J. Chem. Soc. Chem. Commun. 462–463.
González, R.I., Ramírez, R., Rogan, J., Valdivia, J.A., Munoz, F., Valencia, F., Ramírez, M., Kiwi, M., 2014. Model for self-rolling of an aluminosilicate sheet into a single-walled imogolite nanotube. J. Phys. Chem. C 118, 28227–28233.
Gregg, S.J., Sing, K.S.W., 1982. Adsorption, Surface Area and Porosity, 2nd ed. Academic Press, New York.
Harsh, J., 2012. Poorly crystalline aluminosilicate clay minerals. In: Huang, P.M., Li, Y., Sumner, M.E. (Eds.), Handbook of Soil Sciences. CRC Press, Boca Raton, FL (pp. 23.21–23.13).
Harsh, J., Chorover, J., Nizeyimana, E., 2002. Allophane and imogolite. In: Dixon, J.B., Schulze, D.G. (Eds.), Soil Mineralogy with Environmental Applications. Soil Science Society of America, Madison, pp. 291–322.
Hiradate, S., Wada, S.-I., 2005. Weathering process of volcanic glass to allophane determined by 27Al and 29Si solid-state NMR. Clay Clay Miner. 53, 401–408.
Imamura, S., Hayashi, Y., Kajiwara, K., Hoshino, H., Kaito, C., 1993. Imogolite: a possible new type of shape-selective catalyst. Ind. Eng. Chem. Res. 32, 600–603.
Kang, D.-Y., Brunelli, N.A., Yucelen, G.I., Venkatasubramanian, A., Zang, J., Leisen, J., Hesketh, P.J., Jones, C.W., Nair, S., 2014. Direct synthesis of single-walled aminoaluminosilicate nanotubes with enhanced molecular adsorption selectivity. Nat. Commun. 5, 3342.
Kang, D.-Y., Tong, H.M., Zang, J., Choudhury, R.P., Sholl, D.S., Beckham, H.W., Jones, C.W., Nair, S., 2012. Single-walled aluminosilicate nanotube/poly (vinyl alcohol) nanocomposite membranes. ACS Appl. Mater. Interfaces 4, 965–976.
Kang, D.-Y., Zang, J., Wright, E.R., McCanna, A.L., Jones, C.W., Nair, S., 2010. Dehydration, dehydroxylation, and rehydroxylation of single-walled aluminosilicate nanotubes. ACS Nano 4, 4897–4907.
Lee, H., Jeon, Y., Lee, Y., Lee, S.U., Takahara, A., Sohn, D., 2014. Thermodynamic control of diameter-modulated aluminosilicate nanotubes. J. Phys. Chem. C 118, 8148–8152.
Lee, S.U., Choi, Y.C., Youm, S.G., Sohn, D., 2011. Origin of the strain energy minimum in imogolite nanotubes. J. Phys. Chem. C 115, 5226–5231.
Levard, C., Basile-Doelsch, I., 2016. Geology and mineralogy of imogolite-type materials. In: Yuan, P., Thill, A., Bergaya, F. (Eds.), Nanosized Tubular Clay Minerals. Elsevier, Amsterdam, pp. 49–65.
Levard, C., Doelsch, E., Basile-Doelsch, I., Abidin, Z., Miche, H., Masion, A., Rose, J., Borschneck, D., Bottero, J.Y., 2012. Structure and distribution of allophanes, imogolite and proto-imogolite in volcanic soils. Geoderma 183, 100–108.
Levard, C., Rose, J., Thill, A., Masion, A., Doelsch, E., Maillet, P., Spalla, O., Olivi, L., Cognigni, A., Ziarelli, F., 2010. Formation and growth mechanisms of imogolite-like aluminogermanate nanotubes. Chem. Mater. 22, 2466–2473.
Li, D., Nielsen, M.H., Lee, J.R., Frandsen, C., Banfield, J.F., De Yoreo, J.J., 2012. Direction-specific interactions control crystal growth by oriented attachment. Science 336, 1014–1018.
Ma, W., Otsuka, H., Takahara, A., 2011. Poly(methyl methacrylate) grafted imogolite nanotubes prepared through surface-initiated ARGET ATRP. Chem. Commun. 47, 5813–5815.
Maillet, P., Levard, C., Larquet, E., Mariet, C., Spalla, O., Menguy, N., Masion, A., Doelsch, E., Rose, J., Thill, A., 2010. Evidence of double-walled Al-Ge imogolite-like nanotubes. A Cryo-TEM and SAXS investigation. J. Am. Chem. Soc. 132, 1208–1209.
Maillet, P., Levard, C., Spalla, O., Masion, A., Rose, J., Thill, A., 2011. Growth kinetic of single and double-walled aluminogermanate imogolite-like nanotubes: an experimental and modeling approach. Phys. Chem. Chem. Phys. 13, 2682–2689.
Mukherjee, S., Bartlow, V.M., Nair, S., 2005. Phenomenology of the growth of single-walled aluminosilicate and aluminogermanate nanotubes of precise dimensions. Chem. Mater. 17, 4900–4909.
Mukherjee, S., Kim, K., Nair, S., 2007. Short, highly ordered, single-walled mixed-oxide nanotubes assemble from amorphous nanoparticles. J. Am. Chem. Soc. 129, 6820–6826.
Ohashi, F., Tomura, S., Akaku, K., Hayashi, S., Wada, S.I., 2004. Characterization of synthetic imogolite nanotubes as gas storage. J. Mater. Sci. 39, 1799–1801.
Ookawa, M., Inoue, Y., Watanabe, M., Suzuki, M., Yamaguchi, T., 2006. Synthesis and characterization of Fe containing imogolite. Clay Sci. 12, 280–284.
Paineau, E., Krapf, M.-E.M., Amara, M.-S., Matskova, N.V., Dozov, I., Rouzière, S., Thill, A., Launois, P., Davidson, P., 2016. A liquid-crystalline hexagonal columnar phase in highly-dilute suspensions of imogolite nanotubes. Nat. Commun. 7, 10271.
Parfitt, R., 2009. Allophane and imogolite: role in soil biogeochemical processes. Clay Miner. 44, 135–155.
Parfitt, R.L., 1990. Allophane in New-Zealand – a review. Aust. J. Soil Res. 28, 343–360.
Poli, E., Elliott, J., Ratcliff, L.E., Andrinopoulos, L., Dziedzic, J., Hine, N., Mostofi, A.A., Skylaris, C.-K., Haynes, P.D., Teobaldi, G., 2016. The potential of imogolite nanotubes as (co-)photocatalysts: a linear-scaling density functional theory study. J. Phys. Condens. Matter 28, 074003.
Rouquerol, J., Llewellyn, P., Rouquerol, F., 2007. Is the BET equation applicable to microporous adsorbents? Stud. Surf. Sci. Catal. 160, 49–56.
Russell, J., McHardy, W., Fraser, A., 1969. Imogolite: a unique aluminosilicate. Clay Miner. 8, 87–99.
Suzuki, M., Ohashi, F., Inukai, K., Maeda, M., Tomura, S., 2000. Synthesis of allophane and imogolite from inorganic solution: influence of co-existing ion concentration and titration rate on forming precursor. J. Clay Sci. Soc. Jpn. 40, 1–14.
Thill, A., 2016. Characterisation of imogolite by microscopic and spectroscopic methods. In: Yuan, P., Thill, A., Bergaya, F. (Eds.), Nanosized Tubular Clay Minerals. Elsevier, Amsterdam, pp. 223–253.
Thill, A., Picot, P., Belloni, L., 2017. A mechanism for the sphere/tube shape transition of nanoparticles with an imogolite local structure (imogolite and allophane). Appl. Clay Sci. 141, 308–315.
Thommes, M., Kaneko, K., Neimark, A.V., Olivier, J.P., Rodriguez-Reinoso, F., Rouquerol, J., Sing, K.S., 2015. Physisorption of gases, with special reference to the evaluation of surface area and pore size distribution (IUPAC Technical Report). Pure Appl. Chem. 87, 1051–1069.
Wada, K., 1989. Allophane and imogolite. In: Dixon, J.B., Weed, S.B. (Eds.), Minerals in Soil Environments. Soil Science Society of America, Madison, pp. 1051–1087.
Wada, K., Yoshinag, N., 1969. Structure of imogolite. Am. Mineral. 54, 50–71.
Wada, S., Wada, K., 1982. Effects of substitution of germanium for silicon in imogolite. Clay Clay Miner. 30, 123–128.
Wilson, M.A., Lee, G.S.H., Taylor, R.C., 2001. Tetrahedral rehydration during imogolite formation. J. Non-Cryst. Solids 296, 172–181.
Yamamoto, K., Otsuka, H., Takahara, A., 2007. Preparation of novel polymer hybrids from imogolite nanofiber. Polym. J. 39, 1–15.
Yoshinaga, N., Aomine, S., 1962. Imogolite in some Ando soils. Soil Sci. Plant Nutr. 8, 22–29.
Yuan, P., Southon, P.D., Liu, Z.W., Green, M.E.R., Hook, J.M., Antill, S.J., Kepert, C.J., 2008. Functionalization of halloysite clay nanotubes by grafting with gamma-aminopropyltriethoxysilane. J. Phys. Chem. C 112, 15742–15751.
Yuan, P., Tan, D.Y., Bergaya, F., 2015. Properties and applications of halloysite nanotubes: recent research advances and future prospects. Appl. Clay Sci. 112, 75–93.
Yucelen, G.I., Choudhury, R.P., Leisen, J., Nair, S., Beckham, H.W., 2012a. Defect structures in aluminosilicate single-walled nanotubes: a solid-state nuclear magnetic resonance investigation. J. Phys. Chem. C 116, 17149–17157.
Yucelen, G.I., Choudhury, R.P., Vyalikh, A., Scheler, U., Beckham, H.W., Nair, S., 2011. Formation of single-walled aluminosilicate nanotubes from molecular precursors and curved nanoscale intermediates. J. Am. Chem. Soc. 133, 5397–5412.
Yucelen, G.I., Kang, D.-Y., Guerrero-Ferreira, R.C., Wright, E.R., Beckham, H.W., Nair, S., 2012b. Shaping single-walled metal oxide nanotubes from precursors of controlled curvature. Nano Lett. 12, 827–832.
Yucelen, G.I., Kang, D.-Y., Schmidt-Krey, I., Beckham, H.W., Nair, S., 2013. A generalized kinetic model for the formation and growth of single-walled metal oxide nanotubes. Chem. Eng. Sci. 90, 200–212.
Zhang, Y., Tang, A., Yang, H., Ouyang, J., 2016. Applications and interfaces of halloysite nanocomposites. Appl. Clay Sci. 119, 8–17.